Mohamed Zanaty[1]
Instant-Lab,
Institute of Microengineering,
Ecole Polytechnique Fédérale de
Lausanne (EPFL),
Rue de la Maladiere,
Neuchâtel 2000, Switzerland
e-mail: mohamed.zanaty@epfl.ch

Ilan Vardi
Instant-Lab,
Institute of Microengineering,
Ecole Polytechnique Fédérale de
Lausanne (EPFL),
Rue de la Maladiere,
Neuchâtel 2000, Switzerland
e-mail: ilan.vardi@epfl.ch

Simon Henein
Instant-Lab,
Institute of Microengineering,
Ecole Polytechnique Fédérale de
Lausanne (EPFL),
Rue de la Maladiere,
Neuchâtel 2000, Switzerland
e-mail: simon.henein@epfl.ch

Programmable Multistable Mechanisms: Synthesis and Modeling

Compliant mechanisms can be classified according to the number of their stable states and are called multistable mechanisms if they have more than one stable state. We introduce a new family of mechanisms for which the number of stable states is modified by programming inputs. We call such mechanisms programmable multistable mechanisms (PMM). A complete qualitative analysis of a PMM, the T-mechanism, is provided including a description of its multistability as a function of the programming inputs. We give an exhaustive set of diagrams illustrating equilibrium states and their stiffness as one programming input varies while the other is fixed. Constant force behavior is also characterized. Our results use polynomial expressions for the reaction force derived from Euler–Bernoulli beam theory. Qualitative behavior follows from the evaluation of the zeros of the polynomial and its discriminant. These analytical results are validated by numerical finite element method simulations. [DOI: 10.1115/1.4038926]

1 Introduction and Statement of Results

Compliant mechanisms perform a function by their elastic deformation via *actuation inputs*. Their qualitative behavior can be characterized by their stable states where strain energy is minimal, and *multistable mechanisms* are those having more than one stable state, and the number of the stable states is called degree of stability (DOS). Conventional multistable mechanisms have a fixed DOS. In this paper, we examine a family of multistable mechanisms, programmable multistable mechanisms (PMM), where *programming inputs* can modify their DOS. Section 2 gives an overview of PMMs.

In Sec. 3, we introduce a method for synthesizing PMMs which we use to build the main mechanism of this paper, the T-mechanism, as described in Sec. 4. Section 5 gives an analytical derivation of the reaction force of this mechanism as a polynomial of the actuation input. This expression allows us to characterize the stability behavior of the T-mechanism based on the zeros of the reaction force polynomial and its discriminant.

Section 6 provides a complete description of the stability behavior of the T-mechanism in terms of its programming inputs. This consists of the *programming diagram* illustrating DOS as function of programming inputs and *equilibrium and zero stiffness diagrams*, where one programming input is varied and the other is fixed.

Finally, Sec. 7 gives numerical validation of our analytical results using the finite element method (FEM).

2 Programmable Multistable Mechanisms

2.1 Conventional Multistable Mechanisms. Conventional multistable mechanisms are those having fixed stability behavior. They have application to energy harvesting [1,2], radio frequency switches [3], and medical instrumentation [4].

Examples are orthogonal beam mechanisms [5,6], serial multistable mechanisms [7], tristable four bar mechanisms [7], five bar tristable mechanisms [8], Sarrus multistable mechanisms [9], double Young tristable mechanism [10], and rolling contact multistable mechanisms based on nonuniform cams [11].

Multistable mechanisms utilizing the nonlinear interaction between electrostatic and electromagnetic forces were developed in Refs. [3] and [12].

Synthesis of multistable mechanisms has been done by parallel and serial connection of bistable mechanisms [7,10]. A classification of multistable mechanisms based on their kinematics and their strain energy was presented in Ref. [13].

2.2 Definitions. The stability behavior of multistable mechanisms can be characterized in terms of reaction force which is related to the strain energy and stiffness. We give formal definitions to make these concepts as precise as possible.

(1) Our mechanisms have 1DOF, an actuation input x, assumed to be a linear displacement.
(2) $E(x)$ is the *strain energy*, the energy stored in the mechanism due to its elastic deformation.
(3) *Reaction force* is the component of mechanism restoring force along the direction of its displacement x and is given by

$$F = \frac{dE}{dx} \tag{1}$$

Note that according to our definition, reaction force is a scalar.
(4) Secant stiffness is defined by

$$k_s = \frac{F}{x} \tag{2}$$

(5) Tangential stiffness is defined by

[1]Corresponding author.

Contributed by the Mechanisms and Robotics Committee of ASME for publication in the JOURNAL OF MECHANICAL DESIGN. Manuscript received August 12, 2017; final manuscript received December 8, 2017; published online February 5, 2018. Assoc. Editor: Massimo Callegari.

$$k_t = \frac{dF}{dx} \quad (3)$$

Remark. Secant stiffness is used for the derivation of reaction force in Sec. 5 and tangential stiffness is used the evaluation of zero stiffness positions in Sec. 6. The difference between the two stiffness values is explained in Ref. [14].

(6) *Equilibrium positions* are values of the actuation input at which the reaction force is zero. In the generic case, an equilibrium position is *stable* when its tangential stiffness is positive and *unstable* when it is negative. This paper only deals with this generic case, see Ref. [15] for details.

(7) Degree of stability is the number of distinct stable states of a multistable mechanism (not considered with multiplicity).

(8) We call a 1DOS mechanism *monostable*, a 2DOS mechanism *bistable*, a 3DOS mechanism *tristable*, and a 4DOS mechanism *quadrastable*.

2.3 Multistability Programming. Programmable multistable mechanisms are $(N+1)$DOF mechanisms with one actuation input and N programming inputs, where N is the degree of programming (DOP).

The stability behavior of these mechanisms with respect to their actuation input can be modified on varying the programming inputs.

Figure 1 gives a block diagram representation of a 3DOP multistable mechanism and illustrates the effect of the programming inputs on its strain energy. The mechanism can be programmed to be monostable or bistable. Programming inputs can be mechanically imposed as done here or controlled via an electric current, magnetic field or pressure.

The best previously known programmable bistable mechanism (PBM) is the axially loaded beam in which axial load switches monostability to bistability [16,17]; our paper generalizes this concept. Previous work has also considered electrically modified axial load [18], so the results of our paper are not limited to mechanical programming.

A special PMM exhibiting monostability up to quadrastability was applied to ocean wave energy harvesting [2], and bistable Miura origami mechanisms were connected serially to produce PMMs [20]. These papers do not provide an analysis of the effect of the programming inputs on DOS, position of equilibrium states, zero stiffness states, and the stiffness of stable states as is done in our paper.

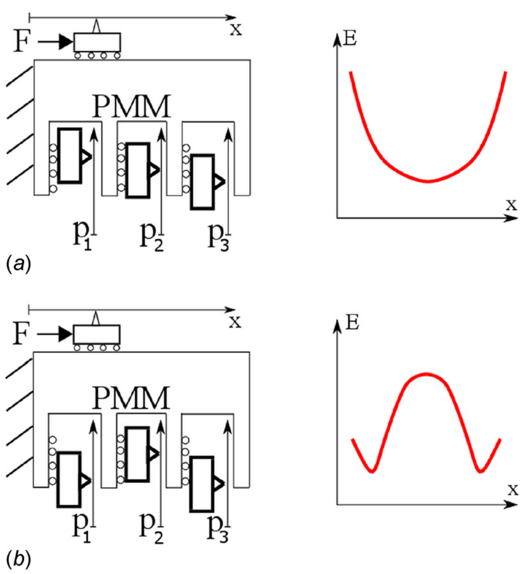

Fig. 1 Block diagram representation of a 3DOP PMM programmed to be (*a*) monostable and (*b*) bistable

The main results of this paper are as follows:

(1) Generic methods for synthezing PMMs.
(2) Definition of parameters characterizing PMMs.
(3) An explicit analytical modeling of 2DOP T-connected PMMs.
(4) Analytical estimate of PMM constant force regimes.

3 Synthesis

3.1 General Method. Programmable multistable mechanisms can be synthesized by combining PBM to obtain a DOS ≥ 2. This method consists of two steps as illustrated in Fig. 2: the first step is *bistability programming* where PBMs are constructed, and the second step is combining these PBMs. This method can be simply applied to any bistable mechanism in literature.

Bistability programming refers to the process of introducing a programming input to a monostable mechanism to produce a PBM. We then combine these PBMs.

The 2DOP T-combination is the connection where the base of one PBM is connected to the actuation block of the other such the actuation directions are orthogonal, as illustrated in Fig. 3.

3.2 Basic Example. A simple example of PBM is the double parallelogram mechanism (DPM) shown in Figs. 4 and 5(*a*). It consists of two horizontal beams centrally connected by the actuation block where the actuation input x is imposed. The beams are fixed at one extremity and axially guided at the other extremity where the programming input p is applied.

The T-combination of two DPMs is shown in Fig. 5(*b*). This mechanism can be programmed to be monostable, bistable, tristable, and quadrastable, as shown in Fig. 6.

3.3 T-Connection Versus Serial and Parallel Connections. Methods for connecting PBMs are the T-connection and the well-known serial and parallel connections (see Fig. 7); the parallel connection is only applicable to tension-based bistable mechanisms [10,20].

This paper focuses on the T-connection since it has five distinct stability regions whereas the serial and parallel connections only have four. The T-mechanism has drawbacks, the stiffness of the bistable module depends on its driving bistable module (see Secs. 4 and 5); so the size of the mechanism increases faster with increasing DOS as compared to serial and parallel configurations.

4 T-Mechanism

The main focus of this paper is the *T-mechanism* shown in Fig. 8 (see Fig. 18 for a three-dimensional FEM rendering). It is a refinement of the basic example of Sec. 3.2 where a spring is used to load axially the horizontal DPM.

We call the horizontal DPM *module 1,* with beams of length ℓ_1, width w and thickness t_1 and the vertical DPM *module 2,* with beams of length ℓ_2, width w, and thickness t_2. Module 1 is axially loaded by a parallelogram spring with beams of length ℓ_r, width w, and thickness t_r, as shown in Fig. 8(*c*). We call this spring the *programming spring*.

4.1 Operation of the Mechanism. The T-mechanism of Fig. 8 has one actuation input x and two programming inputs p_1, p_2. The actuation block of module 2 is displaced transversely by x. In its axial direction, module 2 is displaced by λ_2 at one extremity and has axial load N_2. It is axially displaced by p_2 at its other extremity.

Since the two modules are T-combined, module 1 is displaced transversely by λ_2. In its axial direction, module 1 is displaced by λ_1 under axial load N_1.

The programming spring is loaded transversely by the displacement p_1 which imposes an axial load N_1 on module 1.

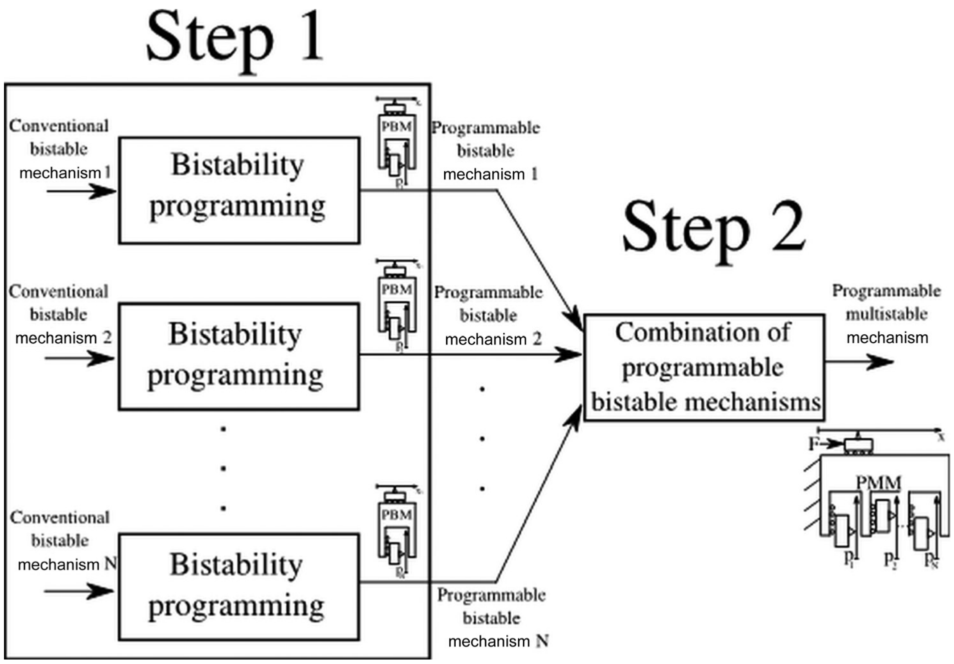

Fig. 2 Synthesis of PMMs

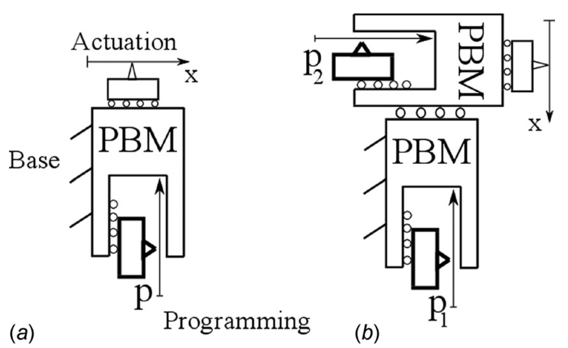

Fig. 3 Block diagram representation of (*a*) PBM and (*b*) 2DOP T-combination

Multistability programming of the T-mechanism relies on DPM buckling imposed by the programming inputs p_1, p_2.

If p_1, p_2 are both smaller than the critical buckling loads p_1^{cr} and p_2^{cr} of modules 1 and 2, respectively, the mechanism is monostable.

If $p_1 < p_1^{cr}$ and $p_2 > p_2^{cr}$, only module 2 buckles and the mechanism is bistable.

If $p_1 > p_1^{cr}$, the mechanism can be monostable, bistable, tristable, or quadrastable depending on p_2. There are values p_2^a, p_2^b, with $p_2^a < p_2^b$, such that:

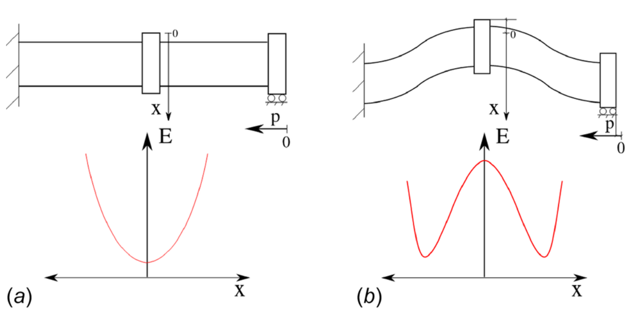

Fig. 4 Double parallelogram mechanism and its strain energy when programmed to be (*a*) monostable and (*b*) bistable

If $p_2 < p_2^a$, the mechanism is monostable; if $p_2^a < p_2 < p_2^b$, the mechanism is bistable; if $p_2^b < p_2 < p_2^{cr}$, the mechanism is tristable and quadrastable when $p_2 > p_2^{cr}$.

The physical significance of p_2^a and p_2^b is that module 1 is known to buckle when $p_1 > p_1^{cr}$ and has three equilibrium states at $\lambda_2 = \lambda_2^a, \lambda_2^b, \lambda_2^c$, where $\lambda_2^a < \lambda_2^b < \lambda_2^c$ with λ_2^a, λ_2^c stable and λ_2^b unstable, see Ref. [14]. Then $p_2^a = \lambda_2^a, p_2^b = \lambda_2^b$, as follows from Eq. (7) at $x = 0$.

Remark. If $p_2^{cr} > p_2^b$, the mechanism cannot be tristable or quadrastable. Moreover, p_2^a, p_2^b, p_2^{cr} depend on p_1.

4.2 Dimensions of the Mechanism.

The relative dimensions of module 1, module 2, and the programming spring determine the values of p_1^{cr}, p_2^a, p_2^b, p_2^{cr} and the possible DOS.

We use the following dimensionless parameters to represent the relative dimensions of the T-mechanism:

- Stiffness ratio of module 1: $\eta_1 = I_r \ell_1^3 / (I_1 \ell_r^3)$.
- Stiffness ratio of module 2: $\eta_2 = I_1 \ell_2^3 / (I_2 \ell_1^3)$.
- Length ratio of module 2: $\alpha_2 = \ell_2 / \ell_1$.

In order to fully illustrate multistability programming, we choose η_1, η_2, α_2 so that the T-mechanisms can exhibit monostable, bistable, tristable, or quadrastable behavior. Figure 9

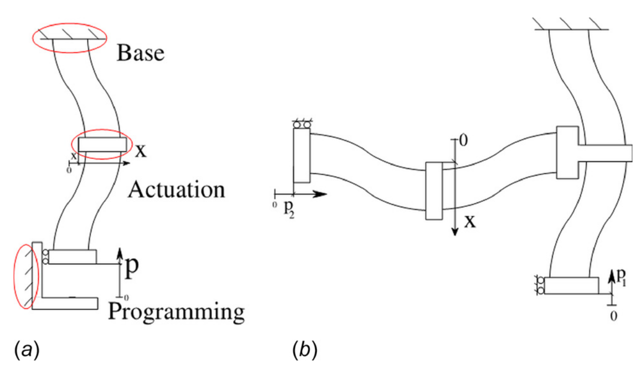

Fig. 5 (*a*) Double parallelogram mechanism connection blocks and (*b*) 2DOP T-combination of DPMs

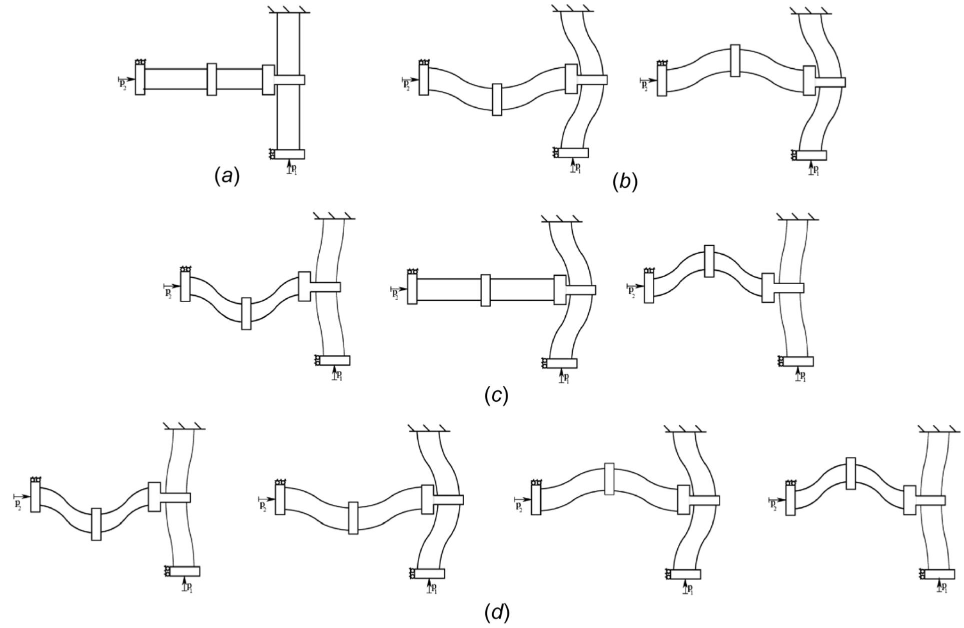

Fig. 6 Stable states of the 2DOP T-mechanism programmed to be (*a*) monostable, (*b*) bistable, (*c*) tristable, and (*d*) quadrastable

illustrates possible DOS for a range of η_1, η_2, and different values of α_2. These values satisfy the conditions of Euler–Bernoulli theory, and we believe that the computations of this paper hold for the values given in Fig. 9(*b*), see Ref. [21]; we refer to the range of values given in this figure as *admissible* η_1, η_2.

In the main example of this paper, we select the physical dimensions $\ell_1 = 12(\mathrm{mm}), \ell_2 = 12(\mathrm{mm}), \ell_r = 3(\mathrm{mm}), t_1 = 100(\mu\mathrm{m})$, $t_2 = 60(\mu\mathrm{m}), t_r = 140(\mu\mathrm{m}), w = 3(\mathrm{mm})$ with Young's modulus $Y = 210(\mathrm{GPa})$. This gives $\eta_1 = 176, \eta_2 = 4.6, \alpha_2 = 1$, the point highlighted in Fig. 9(*b*).

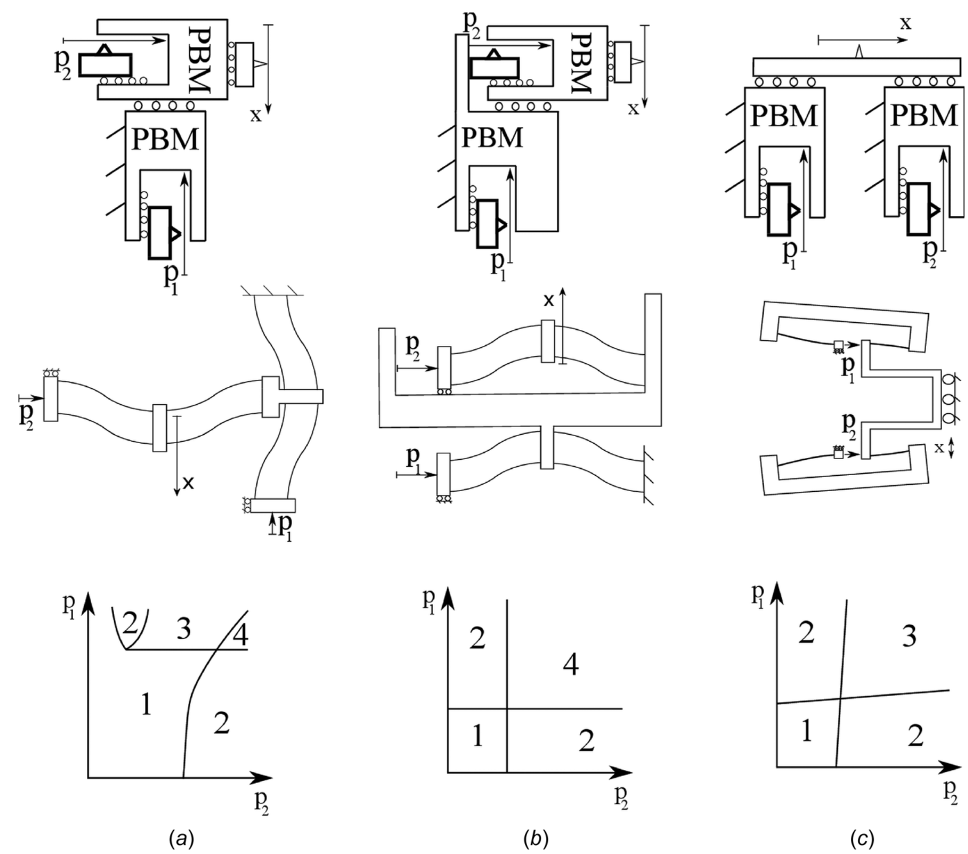

Fig. 7 Block diagram representation, example mechanism and DOS diagram of (*a*) T-connection, (*b*) serial connection, and (*c*) parallel connection

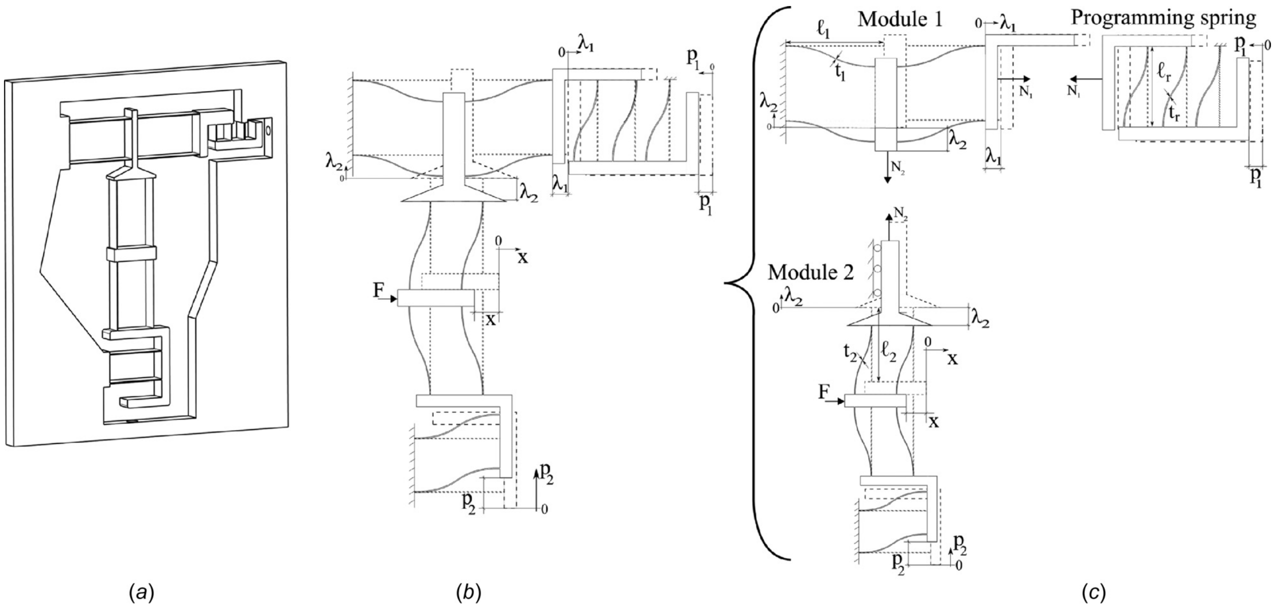

Fig. 8 (*a*) Constructed T-mechanism, (*b*) top view, and (*c*) main components

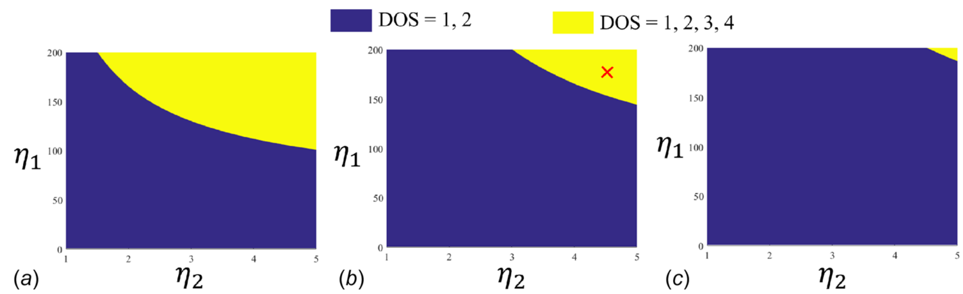

Fig. 9 Range of DOS for admissible η_1, η_2 for (*a*) $\alpha_2 = 0.5$, (*b*) $\alpha_2 = 1$, and (*c*) $\alpha_2 = 1.5$

5 Analytical Model

In this section, we derive the strain energy and the reaction force of the T-mechanism based on Euler–Bernoulli theory [22]. The model is valid under the following assumptions, referring to Fig. 8:

(1) A linear elastic material is used.
(2) Beam length is greater than beam thickness so that shear strain can be neglected.
(3) Actuation force F is applied to the center of the central block of module 2.
(4) Module 2 is connected to the central block of module 1.
(5) Axial shortening of module 1 is an order of magnitude less than the axial shortening of module 2, i.e., $\lambda_1 \ll \lambda_2$.
(6) The displacement range of mechanism is within its intermediate range [13].
(7) Axial load of each blade is inferior to its buckling load with both ends fixed against rotation.

Our analysis consists of the following steps:

(1) Compute the zero load stiffness and zero stiffness load of DPMs of the T-mechanism in terms of their dimensions and the material properties.
(2) Express the relation between the axial shortening λ_1, λ_2 and the programming inputs p_1, p_2 and the actuation input x.
(3) Calculate the axial load N_1 imposed on module 1 as function of p_1, p_2, x.
(4) Calculate the secant stiffness $k_s^{p_1}$ of module 1 based on the axial load N_1 in terms of its zero load stiffness and zero stiffness load.
(5) Calculate the axial load N_2 applied on module 2 as function of p_1, p_2, x.
(6) Calculate the secant stiffness k_s of the T-mechanism, equal to the secant stiffness $k_s^{p_2}$ of module 2.
(7) Calculate the reaction force of the T-mechanism using Hooke's law, $F = k_{sx}$.
(8) Calculate the strain energy of the T-mechanism by integrating its reaction force with respect to displacement.
(9) Define dimensionless mechanism parameters.
(10) Calculate the zero load stiffness and zero stiffness load in terms of dimensionless parameters.
(11) Derive dimensionless reaction force and tangential stiffness in terms of dimensionless parameters.
(12) Express dimensionless reaction force and tangential stiffness in terms of cubic polynomials.

5.1 Zero Load Stiffness and Zero Stiffness Load. *Zero load stiffness* is the secant stiffness of the mechanism at zero axial load. The zero load stiffness k_0^{p1} of module 1 and $k_0^{p_2}$ of module 2 are [14]

$$k_0^{p_1} = \frac{48YI_1}{\ell_1^3}, \quad k_0^{p_2} = \frac{48YI_2}{\ell_2^3} \tag{4}$$

where Y is Young's modulus of the beams, $I_1 = wt_1^3/12$ and $I_2 = wt_2^3/12$ are the second moment of inertia of the beams of module 1 and module 2, respectively.

Zero stiffness load is the axial load at which the secant stiffness of the mechanism is zero. The zero stiffness loads $N_0^{p_1}$ of module 1 and $N_0^{p_2}$ of module 2 are [14]

$$N_0^{p_1} = \frac{2\pi^2 YI_1}{\ell_1^2}, \quad N_0^{p_2} = \frac{2\pi^2 YI_2}{\ell_2^2} \tag{5}$$

The secant stiffness k_s^r of the programming spring is well-approximated by [14]

$$k_s^r = \frac{24YI_r}{\ell_r^3} \tag{6}$$

where it is assumed that the axial load has a negligible effect on the stiffness of the programming spring.

5.2 Axial Shortening. The axial shortening of module 2 is [14]

$$\lambda_2 = p_2 - \frac{6x^2}{5\ell_2} \tag{7}$$

Since module 1 and module 2 are T-combined, the axial displacement of module 2 equals the transverse displacement of module 1, so λ_2 leads to an axial shortening

$$\lambda_1 = -\frac{6\lambda_2^2}{5\ell_1} \tag{8}$$

of module 1. By direct substitution of Eq. (7) into Eq. (8), the axial shortening of module 1 becomes

$$\lambda_1 = -\frac{216}{125\ell_1\ell_2^2}x^4 + \frac{72p_2}{25\ell_1\ell_2}x^2 - \frac{6p_2^2}{5\ell_1} \tag{9}$$

5.3 Axial Loads. Module 1 imposes an axial load N_2 on module 2 as illustrated in Fig. 8. From Hooke's law

$$N_2 = k_s^{p_1}\lambda_2 \tag{10}$$

where $k_s^{p_1}$ is the secant transverse stiffness of module 1 which equals [14]

$$k_s^{p_1} = k_0^{p_1}\left(1 - \frac{\pi^2 N_1}{10N_0^{p_1}}\right) \tag{11}$$

The force N_1 imposed by the programming spring on module 1 depends on p_1 and is calculated using Hooke's law

$$N_1 = k_s^r(p_1 + \lambda_1)$$

By direct substitution from Eq. (9), the axial load on module 1 is

$$N_1 = k_s^r\left(p_1 - \frac{216x^4}{125\ell_1\ell_2^2} + \frac{72p_2x^2}{25\ell_1\ell_2} - \frac{6p_2^2}{5\ell_1}\right) \tag{12}$$

By direct substitution from Eq. (12) into Eq. (11), the transverse stiffness of module 1 is

$$k_s^{p_1} = \left(k_0^{p_1} - \frac{\pi^2 k_0^{p_1}k_s^r p_1}{10N_0^{p_1}} + \frac{6\pi^2 k_0^{p_1}k_s^r p_2^2}{50N_0^{p_1}\ell_1}\right) - \frac{72\pi^2 k_0^{p_1}k_s^r p_2}{250\ell_1\ell_2 N_0^{p_1}}x^2 + \frac{216\pi^2 k_0^{p_1}k_s^r}{1250\ell_1\ell_2^2 N_0^{p_1}}x^4 \tag{13}$$

The axial load N_2 of module 2 is found by direct substitution of Eqs. (7) and (13) into Eq. (10)

$$\begin{aligned} N_2 = {} & \left(k_0^{p_1}p_2 - \frac{\pi^2 k_0^{p_1}k_s^r p_1 p_2}{10N_0^{p_1}} + \frac{6\pi^2 k_0^{p_1}k_s^r p_2^3}{50N_0^{p_1}\ell_1}\right) \\ & - \left(\frac{6k_0^{p_1}}{5\ell_2} - \frac{6\pi^2 k_0^{p_1}k_s^r p_1}{50N_0^{p_1}\ell_2} + \frac{108\pi^2 k_0^{p_1}k_s^r p_2^2}{250N_0^{p_1}\ell_1\ell_2}\right)x^2 \\ & + \frac{648\pi^2 k_0^{p_1}k_s^r p_2}{1250N_0^{p_1}\ell_1\ell_2^2}x^4 - \frac{1296\pi^2 k_0^{p_1}k_s^r}{6250N_0^{p_1}\ell_1\ell_2^3}x^6 \end{aligned} \tag{14}$$

5.4 Secant Stiffness. The secant stiffness k_s of the T-mechanism equals the secant stiffness of module 2

$$k_s = k_s^{p_2} \tag{15}$$

The secant stiffness of module 2 depends on its axial load N_2 [14]

$$k_s^{p_2} = k_0^{p_2}\left(1 - \frac{\pi^2 N_2}{10N_0^{p_2}}\right) \tag{16}$$

By substitution from Eqs. (14) and (15) into Eq. (16), the secant stiffness of the T-mechanism becomes

$$\begin{aligned} k_s^t = {} & \left(k_0^{p_2} - \frac{\pi^2 k_0^{p_2}k_0^{p_1}p_2}{10N_0^{p_2}} + \frac{\pi^4 k_0^{p_2}k_0^{p_1}k_s^r p_1 p_2}{100N_0^{p_2}N_0^{p_1}} - \frac{6\pi^4 k_0^{p_2}k_0^{p_1}k_s^r p_2^3}{500N_0^{p_2}N_0^{p_1}\ell_1}\right) \\ & + \left(\frac{6\pi^2 k_0^{p_2}k_0^{p_1}}{50N_0^{p_2}\ell_2} - \frac{6\pi^4 k_0^{p_2}k_0^{p_1}k_s^r p_1}{500N_0^{p_2}N_0^{p_1}\ell_2} + \frac{108\pi^4 k_0^{p_2}k_0^{p_1}k_s^r p_2^2}{2500N_0^{p_2}N_0^{p_1}\ell_1\ell_2}\right)x^2 \\ & - \frac{648\pi^4 k_0^{p_2}k_0^{p_1}k_s^r p_2}{12{,}500N_0^{p_2}N_0^{p_1}\ell_1\ell_2^2}x^4 + \frac{1296\pi^4 k_0^{p_2}k_0^{p_1}k_s^r}{62{,}500N_0^{p_2}N_0^{p_1}\ell_1\ell_2^3}x^6 \end{aligned} \tag{17}$$

5.5 Reaction Force. The reaction force of the T-mechanism follows Hooke's law

$$F = k_s x$$

Direct substitution from Eq. (17) yields

$$\begin{aligned} F = {} & \left(k_0^{p_2} - \frac{\pi^2 k_0^{p_2}k_0^{p_1}p_2}{10N_0^{p_2}} + \frac{\pi^4 k_0^{p_2}k_0^{p_1}k_s^r p_1 p_2}{100N_0^{p_2}N_0^{p_1}} - \frac{6\pi^4 k_0^{p_2}k_0^{p_1}k_s^r p_2^3}{500N_0^{p_2}N_0^{p_1}\ell_1}\right)x \\ & + \left(\frac{6\pi^2 k_0^{p_2}k_0^{p_1}}{50N_0^{p_2}\ell_2} - \frac{6\pi^4 k_0^{p_2}k_0^{p_1}k_s^r p_1}{500N_0^{p_2}N_0^{p_1}\ell_2} + \frac{108\pi^4 k_0^{p_2}k_0^{p_1}k_s^r p_2^2}{2500N_0^{p_2}N_0^{p_1}\ell_1\ell_2}\right)x^3 \\ & - \frac{648\pi^4 k_0^{p_2}k_0^{p_1}k_s^r p_2}{12{,}500N_0^{p_2}N_0^{p_1}\ell_1\ell_2^2}x^5 + \frac{1296\pi^4 k_0^{p_2}k_0^{p_1}k_s^r}{62{,}500N_0^{p_2}N_0^{p_1}\ell_1\ell_2^3}x^7 \end{aligned} \tag{18}$$

5.6 Strain Energy. The strain energy E of the T-shaped mechanism is the integral of its reaction force F with respect to its displacement x, and integrating Eq. (18) gives

$$\begin{aligned} E = {} & \left(\frac{k_0^{p_2}}{2} - \frac{\pi^2 k_0^{p_2}k_0^{p_1}p_2}{20N_0^{p_2}} + \frac{\pi^4 k_0^{p_2}k_0^{p_1}k_r p_1 p_2}{200N_0^{p_2}N_0^{p_1}} - \frac{3\pi^4 k_0^{p_2}k_0^{p_1}k_r p_2^3}{500N_0^{p_2}N_0^{p_1}\ell_1}\right)x^2 \\ & + \left(\frac{3\pi^2 k_0^{p_2}k_0^{p_1}}{100N_0^{p_2}\ell_2} - \frac{3\pi^4 k_0^{p_2}k_0^{p_1}k_r p_1}{1000N_0^{p_2}N_0^{p_1}\ell_2} + \frac{27\pi^4 k_0^{p_2}k_0^{p_1}k_r p_2^2}{2500N_0^{p_2}N_0^{p_1}\ell_1\ell_2}\right)x^4 \\ & - \frac{27\pi^4 k_0^{p_2}k_0^{p_1}k_r p_2}{3125N_0^{p_2}N_0^{p_1}\ell_1\ell_2^2}x^6 + \frac{81\pi^4 k_0^{p_2}k_0^{p_1}k_r}{31{,}250N_0^{p_2}N_0^{p_1}\ell_1\ell_2^3}x^8 \end{aligned} \tag{19}$$

where the constant of integration is set to zero, since we are only interested in strain energy difference.

5.7 Normalization. Normalization enables our analysis to be independent of physical dimensions. We introduce the following dimensionless parameters:

(1) actuation input $\hat{x} = x/\ell_2$,
(2) programming inputs $\hat{p}_1 = p_1/\ell_1, \hat{p}_2 = p_2/\ell_2$,

and dimensionless properties:

(1) secant stiffness $\hat{k}_s = k_s\ell_2^3/(YI_2)$,
(2) reaction force $\hat{F} = F\ell_2^2/(YI_2)$, and
(3) strain energy $\hat{E} = E\ell_2/(YI)$.

Equations (4)–(6) and (17) give

$$\hat{k}_s = \beta_0 + \beta_1\hat{x}^2 + \beta_2\hat{x}^4 + \beta_3\hat{x}^6 \tag{20}$$

where

$$\begin{aligned}
\beta_0 &= 48 - \frac{576\eta_2\hat{p}_2}{5} + \frac{3456\eta_1\eta_2\hat{p}_1\hat{p}_2}{25} - \frac{20{,}736\eta_1\eta_2\alpha_2^2\hat{p}_2^3}{125}\\
\beta_1 &= \frac{3456\eta_2}{25} - \frac{20{,}736\eta_1\eta_2\hat{p}_1}{125} + \frac{36{,}429\eta_1\eta_2\alpha_2^2\hat{p}_2^2}{61}\\
\beta_2 &= -\frac{7883\eta_1\eta_2\alpha_2^2\hat{p}_2}{11}, \beta_3 = \frac{30{,}672\eta_1\eta_2\alpha_2^2}{107}
\end{aligned} \tag{21}$$

Equations (4)–(6) and (18) give (normalized Hooke's law)

$$\hat{F} = \beta_0\hat{x} + \beta_1\hat{x}^3 + \beta_2\hat{x}^5 + \beta_3\hat{x}^7 \tag{22}$$

and Eqs. (4)–(6) and (19) give (normalized integration)

$$\hat{E} = \frac{\beta_0}{2}\hat{x}^2 + \frac{\beta_1}{4}\hat{x}^4 + \frac{\beta_2}{6}\hat{x}^6 + \frac{\beta_3}{8}\hat{x}^8 \tag{23}$$

5.8 Reduction to Cubic Polynomial

5.8.1 Reaction Force. The normalized reaction force can be written in terms of a cubic polynomial

$$\hat{F} = \hat{x}\,\Phi(\hat{x}^2) \tag{24}$$

where

$$\Phi(z) = \beta_0 + \beta_1 z + \beta_2 z^2 + \beta_3 z^3, \quad z = x^2 \tag{25}$$

The equilibrium points of $\hat{F}$ are

$$q_0 = 0, \quad q_i^{\pm} = \pm\sqrt{z_i}, \quad i = 1, 2, 3 \tag{26}$$

where z_1, z_2, z_3 are the roots of the polynomial $\Phi(z)$. Note that q_i^+, q_i^- make physical sense only if z_i is real and non-negative.

5.8.2 Tangential Stiffness. The normalized tangential stiffness is

$$\hat{k}_t = \frac{d\hat{F}}{d\hat{x}}$$

so it can be written

$$\hat{k}_t = \Xi(\hat{x}^2) \tag{27}$$

where

$$\Xi(z) = \beta_0 + 3\beta_1 z + 5\beta_2 z^2 + 7\beta_3 z^3, \quad z = x^2 \tag{28}$$

The zero stiffness positions are

$$\zeta_i^{\pm} = \pm\sqrt{z_i}, \quad i = 1, 2, 3 \tag{29}$$

where z_1, z_2, z_3 are the roots of the cubic polynomial $\Xi(z)$. Note that ζ_i^+, ζ_i^- make physical sense only if z_i is real and non-negative.

5.9 Roots of a Cubic Polynomial. The qualitative behavior of the roots of $\Phi(z)$ can be described by its discriminant [23]

$$\Delta_\Phi = 18\beta_3\beta_2\beta_1\beta_0 - 4\beta_2^3\beta_0 + \beta_2^2\beta_1^2 - 4\beta_3\beta_1^3 - 27\beta_3^2\beta_0^2 \tag{30}$$

If Δ_Φ is negative, then Φ has one real root; otherwise, it has three real roots. The sign of the real roots can be determined by *Descarte's rule of signs* which states that the number of positive roots of a polynomial is either equal to the number of sign differences between consecutive nonzero coefficients or is less than it by an even number, and equality holds if all the roots are real [23,24].

5.10 Evaluation of DOS. We use the basic properties of the previous section to compute the DOS, the number of minima of the strain energy E. Since E is an even degree polynomial with $E \to \infty$ as $\hat{x} \to \pm\infty$, it is easily seen that in the generic case

$$\text{DOS} = \frac{n_q + 1}{2} \tag{31}$$

where n_q is the number of equilibrium points. Let n^+ be the number of positive roots of Φ, Eq. (26) shows that $n_q = 2n^+ + 1$, so that

$$\text{DOS} = n^+ + 1 \tag{32}$$

We can now use the discriminant and Descarte's rules of signs to evaluate the DOS as shown in Table 1, where $\sigma(\Delta)$ is the sign of discriminant and n_σ is the number of sign changes of the coefficients of Φ.

6 Qualitative Stability Behavior

For fixed programming inputs $\hat{p}_1$, $\hat{p}_2$, the qualitative stability is given by the strain energy, as shown in Fig. 10 for different programmed DOS. Note that $\hat{x} = 0$ is always an equilibrium state, stable for odd DOS and unstable for even DOS, and the other equilibrium states are symmetric around $\hat{x} = 0$. The rest of this section characterizes qualitative behavior as the programming inputs $\hat{p}_1$, $\hat{p}_2$ vary.

Our explicit analytical computations, including the evaluation of DOS, are summarized in Figs. 11–19 and pertain to the specific values $\eta_1 = 176$, $\eta_2 = 4.6$, and $\alpha_2 = 1$, see Sec. 4.2. We believe that the same qualitative behavior holds for all admissible η_1, η_2, and $\alpha_2 = 1$, see Ref. [21].

Table 1 Evaluation of DOS

$\sigma(\Delta)$	n_σ	DOS
−	0	1
+		1
−	1	2
+		2
−	2	1
+		3
−	3	2
+		4

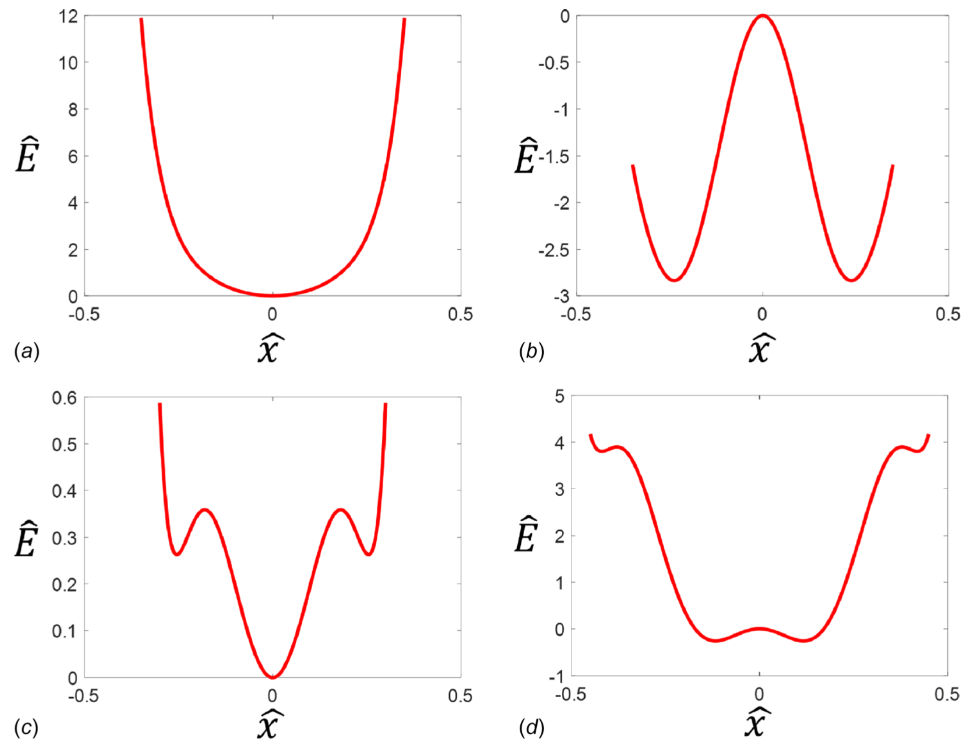

Fig. 10 Strain energy of the T-mechanism programmed to be (*a*) monostable at $\hat{p}_1 = 0, \hat{p}_2 = 0$, (*b*) bistable at $\hat{p}_1 = 0, \hat{p}_2 = 0.12$, (*c*) tristable at $\hat{p}_1 = 0.0175, \hat{p}_2 = 0$, and (*d*) quadrastable at $\hat{p}_1 = 0.12, \hat{p}_2 = 0.0175$

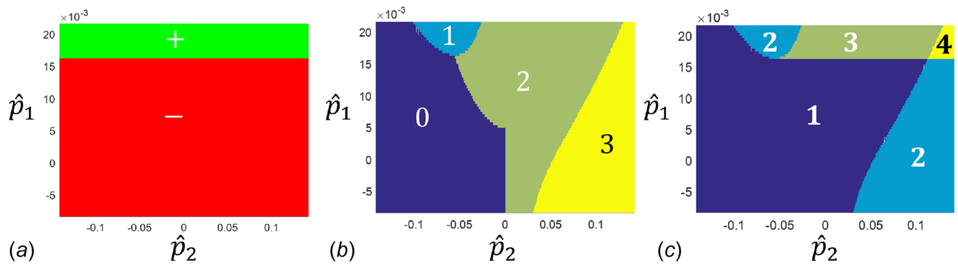

Fig. 11 (*a*) Sign of the discriminant Δ_Φ, (*b*) number of sign alternations n_σ, and (*c*) DOS

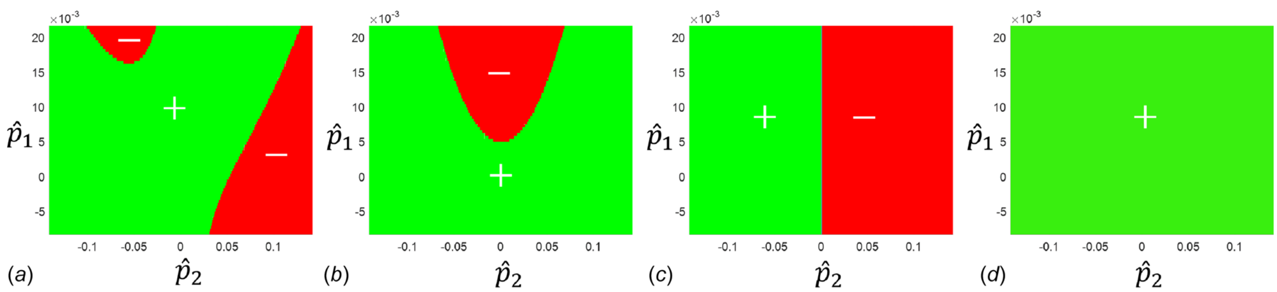

Fig. 12 Sign of (*a*) β_0, (*b*) β_1, (*c*) β_2, and (*d*) β_3

6.1 Computation of DOS of the T-Mechanism. Our main result is the DOS as a function of $\hat{p}_1$, $\hat{p}_2$ illustrated in Fig. 11(*c*) for $\eta_1 = 176$, $\eta_2 = 4.6$, and $\alpha_2 = 1$.

In order to derive this, we begin by considering all admissible η_1, η_2, and $\alpha_2 = 1$. Although the DOS depends on the polynomial Φ defined in Eq. (25), we will show that it can be largely determined by β_0, the constant term of Φ. Indeed, β_0 is the tangential stiffness at $x = 0$, the equilibrium state q_0, and as illustrated in Fig. 10 going from odd DOS to even DOS or vice-versa is equivalent to a change in the sign of β_0, so roots of $\beta_0 = 0$ determine a change of DOS. The values of $\hat{p}_2$ for which β_0 vanishes are $\hat{p}_2^a$, $\hat{p}_2^b$, $\hat{p}_2^{cr}$ and correspond to the buckling described in Sec. 4.1. Figure 13 is an example of how these values delineate regions with different DOS.

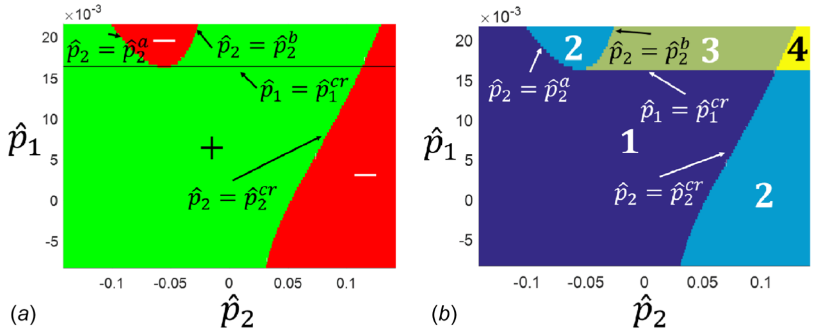

Fig. 13 (*a*) Sign and zeros of β_0 and (*b*) DOS with boundaries

According to Secs. 5.9 and 5.10, the number of real zeros of Φ is determined by the sign of its discriminant

$$\begin{aligned}\Delta_\Phi = &-5111670774.5\eta_1^2\eta_2^2 - 3029140967.2\eta_1\eta_2^4\\ &+10904907482.1\eta_1^2\eta_2^4\hat{p}_1 - 13085888978.5\eta_1^3\eta_2^4\hat{p}_1^2\\ &+5234355591.4\eta_1^4\eta_2^4\hat{p}_1^3 - 29089\eta_1^2\eta_2^3\hat{p}_2 + 34906.8\eta_1^3\eta_2^3 p_1\hat{p}_2\\ &+62870.5\eta_1^2\eta_2^4\hat{p}_2^2 - 150889.0\eta_1^3\eta_2^4\hat{p}_1\hat{p}_2^2 + 90533.5\eta_1^4\eta_2^4\hat{p}_1^2\hat{p}_2^2\\ &+75934.2\eta_1^3\eta_2^3\hat{p}_2^3 - 0.2\eta_1^3\eta_2^4\hat{p}_2^4 + 0.26\eta_1^4\eta_2^4\hat{p}_1\hat{p}_2^4\\ &-0.28\eta_1^4\eta_2^4\hat{p}_2^6\end{aligned} \tag{33}$$

where floating point coefficients highlight approximate behavior.

Equation (33) shows that only the terms *not* involving $\hat{p}_2$ are significant, as illustrated by Fig. 11(*a*), where the positive and negative values of Δ are separated by a horizontal line at $\hat{p}_1 = \hat{p}_1^{cr}$.

To compute $\hat{p}_1^{cr}$, we let Δ_Φ^* be the terms of Δ_Φ not involving $\hat{p}_2$ and find the value $\hat{p}_1^{cr}$ for which $\Delta_\Phi^*(\hat{p}_1^{cr}) = 0$. Dividing Δ_Φ^* by the leading coefficient of $\hat{p}_1^3$ gives the normalized discriminant

$$\begin{aligned}\Delta_\Phi^n = &-0.976562\eta_1^2\eta_2^2 - 0.578704\eta_1\eta_2^4 + 2.08333\eta_1^2\eta_2^4\hat{p}_1\\ &-2.5\eta_1^3\eta_2^4\hat{p}_1^2 + \eta_1^4\eta_2^4\hat{p}_1^3\end{aligned} \tag{34}$$

where $\hat{p}_1^{cr}$ is a root of this polynomial. We now examine β_0 and note that $\beta_0 = B(\hat{p}_2)$, where $B(z)$ is a polynomial with coefficients depending on p_1. The discriminant of B is

$$\begin{aligned}\Delta_B = &-1711891286.1\eta_1^2\eta_2^2 - 1014454095.4\eta_1\eta_2^4\\ &+3652034743.6\eta_1^2\eta_2^4\hat{p}_1 - 4382441692.3\eta_1^3\eta_2^4\hat{p}_1^2\\ &+1752976676.9\eta_1^4\eta_2^4\hat{p}_1^3\end{aligned} \tag{35}$$

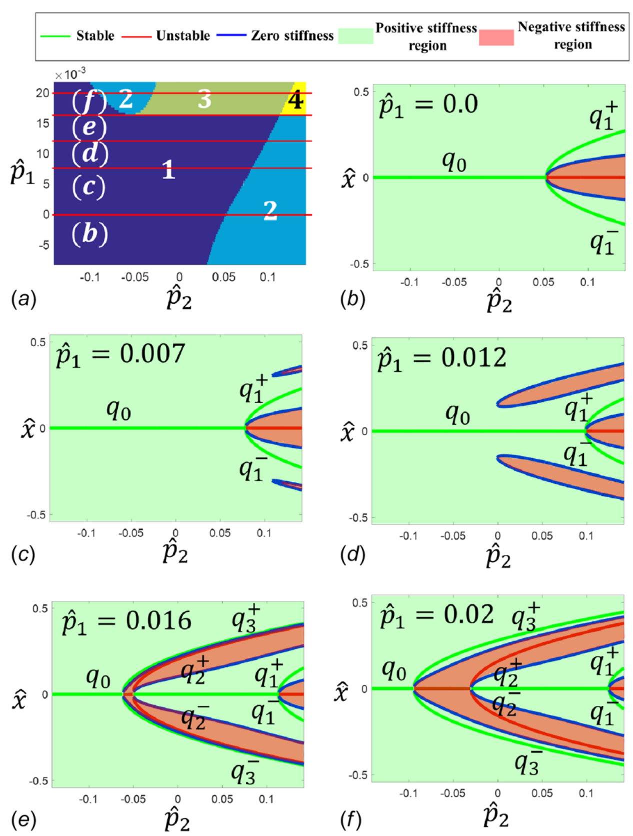

Fig. 14 Equilibrium and zero stiffness diagrams for the fixed values shown in (*a*): (*b*) $\hat{p}_1 = 0.0$, (*c*) $\hat{p}_1 = 0.007$, (*d*) $\hat{p}_1 = 0.012$, (*e*) $\hat{p}_1 = 0.016$, and (*f*) $\hat{p}_1 = 0.02$

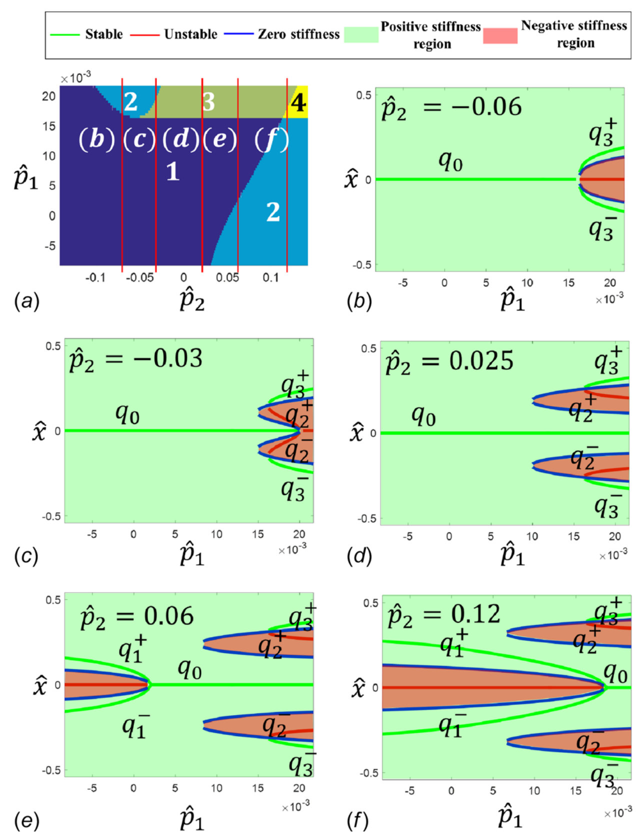

Fig. 15 Equilibrium and zero stiffness diagrams for the fixed values shown in (*a*): (*b*) $\hat{p}_2 = -0.06$, (*c*) $\hat{p}_2 = -0.03$, (*d*) $\hat{p}_2 = 0.025$, (*e*) $\hat{p}_2 = 0.06$, and (*f*) $\hat{p}_2 = 0.12$

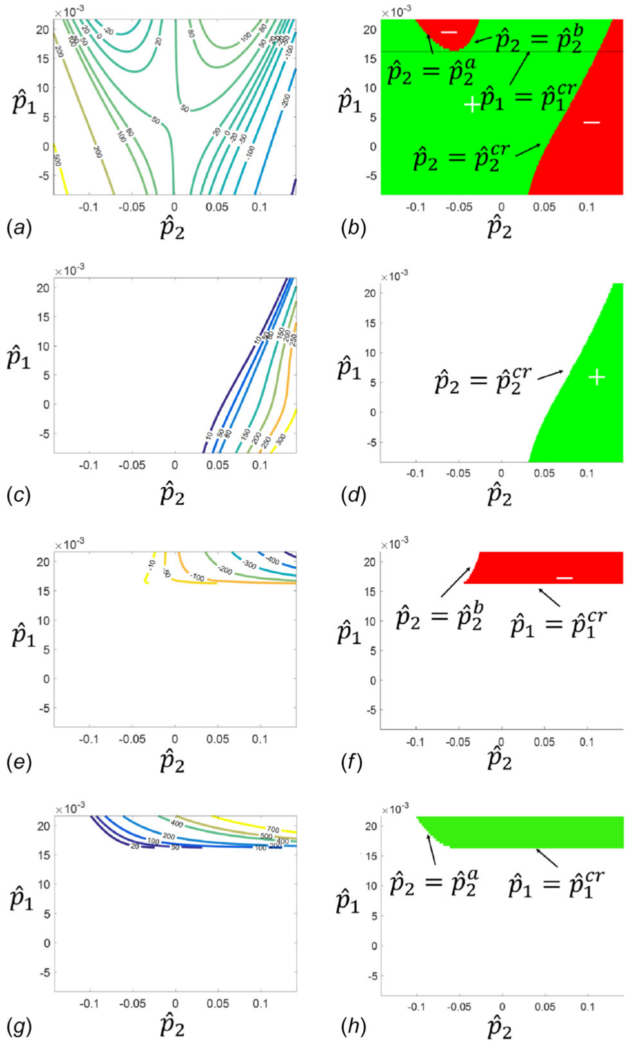

Fig. 16 Stiffness and sign of stiffness at equilibrium positions: (*a*) and (*b*) for q_0, (*c*) and (*d*) for q_1, (*e*) and (*f*) for q_2, (*g*) and (*h*) for q_3

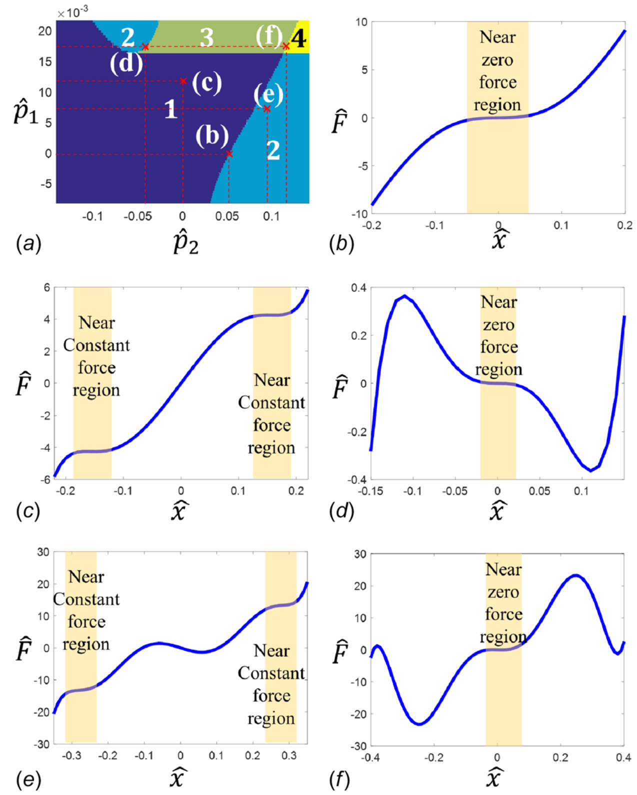

Fig. 17 (*a*) Selected values of $\hat{p}_1$, $\hat{p}_2$ leading to near zero force and near constant force regions: (*b*) zero force monostable mechanism at $\hat{p}_1 = 0, \hat{p}_2 = 0.052$, (*c*) constant force monostable mechanism at $\hat{p}_1 = 0.012, \hat{p}_2 = 0$, (*d*) zero force bistable mechanism at $\hat{p}_1 = 0.017, \hat{p}_2 = -0.045$, (*e*) constant force bistable mechanism at $\hat{p}_1 = 0.007, \hat{p}_2 = 0.092$, and (*f*) zero force tristable mechanism at $\hat{p}_1 = 0.017, \hat{p}_2 = 0.12$

and dividing by the leading coefficient $\hat{p}_1^3$ gives the normalized form

$$\Delta_B^n = -0.976563\eta_1^2\eta_2^2 - 0.578704\eta_1\eta_2^4 + 2.08333\eta_1^2\eta_2^4\hat{p}_1 - 2.5\eta_1^3\eta_2^4\hat{p}_1^2 + \eta_1^4\eta_2^4\hat{p}_1^3 \quad (36)$$

A comparison of Δ_Φ^n and Δ_B^n shows that they only differ in the term $\eta_1^2\eta_2^2$ by one part per million, so for admissible η_1, η_2 and the range of programming values $\hat{p}_1, \hat{p}_2$, the two polynomials can be considered equal with $\Delta_\Phi = 2.98598\Delta_B$. It follows that the real root of Δ_B can be identified with $\hat{p}_1^{cr}$, the root of Δ_Φ. On solving $\Delta_B^n = 0$ using the exact values of β_0 given in Eq. (21), we get

$$\hat{p}_1^{cr} = \frac{5}{6\eta_1} + \frac{126}{127}\left(\frac{1}{\eta_1\eta_2}\right)^{2/3} \quad (37)$$

We conclude that for $\hat{p}_1$ fixed, Φ and β_0 have the same number of real zeros, as $\hat{p}_2$ varies.

The number of coefficient sign alternations of Φ, as $\hat{p}_1, \hat{p}_2$ vary, is computed by the signs of $\beta_0, \beta_1, \beta_2, \beta_3$ shown in Fig. 12 and leads to the number of coefficient sign alternations shown in Fig. 11(*b*). Numerical inspection for our chosen values of $\eta_1 = 176$, $\eta_2 = 4.6$ shows that the regions having an equal number of sign alternations are essentially determined by the sign of

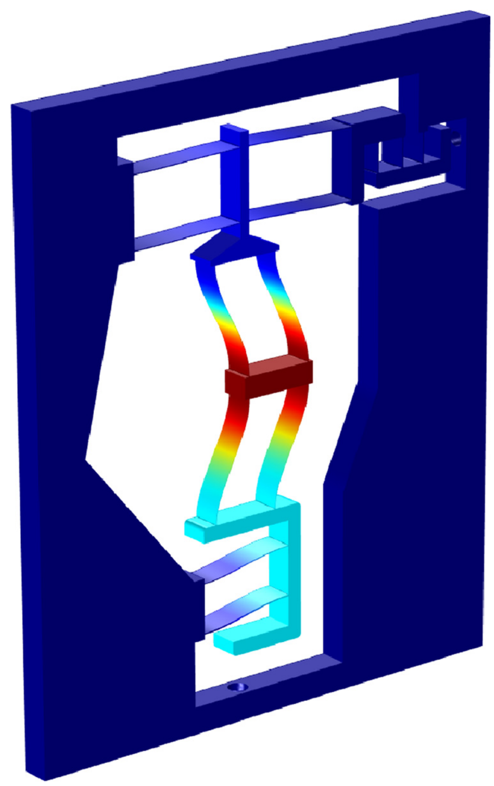

Fig. 18 FEM rendering of T-mechanism deformation

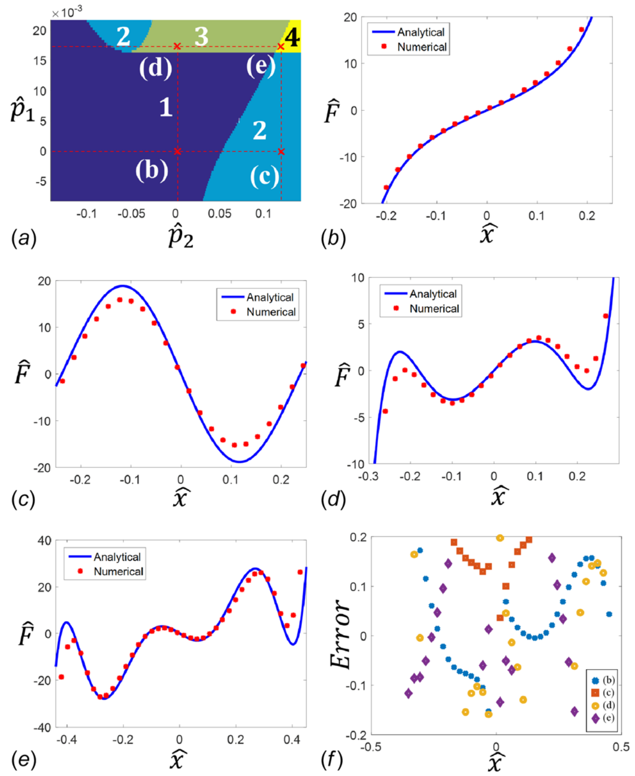

Fig. 19 (a) Values of $\hat{p}_1, \hat{p}_2$ for FEM simulation with T-mechanism programmed to be (b) monostable at $\hat{p}_1 = 0, \hat{p}_2 = 0$, (c) bistable at $\hat{p}_1 = 0, \hat{p}_2 = 0.12$, (d) tristable at $\hat{p}_1 = 0.0175$, $\hat{p}_2 = 0$, (e) quadrastable at $\hat{p}_1 = 0.0175, \hat{p}_2 = 0.012$, and (f) Present difference between analytical and numerical models

β_0, so, as expected, the boundaries between such regions correspond to zeros of β_0 as illustrated in Fig. 13.

6.2 Equilibrium and Zero Stiffness Diagrams. An equilibrium and zero stiffness diagram gives the positions of equilibrium and zero stiffness positions as one programming input is fixed and the other varies. Characteristically, these diagrams exhibit *bifurcation*, see Ref. [15] for the definition of the different types of bifurcation.

Figure 14 gives the equilibrium and zero stiffness diagrams as a function of $\hat{p}_2$ for five different values of $\hat{p}_1$ as illustrated with the programming diagram in Fig. 14(*a*).

Figure 14(*b*) corresponds to $\hat{p}_1 = 0$. For $\hat{p}_2 < \hat{p}_2^{cr}$, where $\hat{p}_2^{cr} = 0.055$, the mechanism is monostable with stable position $q_0 = \hat{x} = 0$. At $\hat{p}_2 = \hat{p}_2^{cr}$, a pitch-fork bifurcation occurs. The stable position q_0 becomes unstable and bifurcates into two stable positions $q_1^{\pm}$. Also, at $\hat{p}_2 = \hat{p}_2^{cr}$, a saddle-node bifurcation occurs for zero stiffness positions.

Figure 14(*c*) corresponds to $\hat{p}_1 = 0.007$. Bifurcation of both equilibrium and zero stiffness occurs at $\hat{p}_2^{cr} = 0.08$ and four new zero stiffness states appear when $\hat{p}_2 > 0.08$.

Figure 14(*d*) corresponds to $\hat{p}_1 = 0.012$ and bifurcation occurs at $\hat{p}_2^{cr} = 0.1$. Note that as $\hat{p}_1$ increases with $\hat{p}_2$ fixed, zero stiffness positions move closer to $\hat{x} = 0$ and bifurcation occurs at a higher $\hat{p}_2^{cr}$.

Figure 14(*e*) corresponds to $\hat{p}_1 = 0.017$. Since $\hat{p}_1 > \hat{p}_1^{cr} = 0.016$, the zero stiffness positions merge and two pitch-fork bifurcations occur at $\hat{p}_2 = \hat{p}_2^{a} = -0.055$ and $\hat{p}_2 = \hat{p}_2^{b} = -0.045$. At $\hat{p}_2 = \hat{p}_2^{a}$, stable position q_0 becomes unstable and bifurcate into two stable states $q_3^{\pm}$. At $\hat{p}_2 = \hat{p}_2^{b}$, unstable position q_0 becomes stable and bifurcates into two unstable positions $q_2^{\pm}$. A pitch fork bifurcation occurs at $\hat{p}_2 = \hat{p}_2^{cr}$, where $\hat{p}_2^{cr} = 0.12$ and q_0 bifurcates into two unstable $q_1^{\pm}$.

Figure 14(*f*) corresponds to $\hat{p}_1 = 0.02$. This figure is qualitatively the same as Fig. 14(*e*), where, for fixed $\hat{p}_2$, positions $q_3^{\pm}$ move apart and $q_1^{\pm}$ move closer. The bifurcation positions $\hat{p}_2^{a}$ and $\hat{p}_2^{b}$ have moved apart.

Similarly, Fig. 15 gives equilibrium and zero stiffness positions for five different values of $\hat{p}_2$, as illustrated in Fig. 15(*a*).

Figure 15(*b*) corresponds to $\hat{p}_2 = -0.06$. The mechanism is monostable for $\hat{p}_1 < \hat{p}_1^{cr}$ with a stable state $q_0 = \hat{x} = 0$. At $\hat{p}_1 = \hat{p}_1^{cr}$, stable position q_0 bifurcates into two stable states $q_3^{\pm}$ and becomes unstable. A saddle node bifurcation occurs for the zero stiffness position at $\hat{p}_1 = \hat{p}_1^{cr}$.

Figure 15(*c*) corresponds to $\hat{p}_2 = -0.03$ with one stable position for $\hat{p}_1 < \hat{p}_1^{cr}$. A saddle node bifurcation occurs at $\hat{p}_1 = \hat{p}_1^{cr}$, where equilibrium states $q_2^{\pm}, q_3^{\pm}$ are created. As illustrated in Sec. 6.1, on increasing $\hat{p}_1$, $\hat{p}_2^{b}$ increases. When $\hat{p}_2^{b} = \hat{p}_2 = -0.03$, a subcritical pitch-fork bifurcation occurs, and the stable state q_0 becomes unstable and bifurcates into two unstable positions $q_2^{\pm}$.

Figure 15(*d*) corresponds to $\hat{p}_2 = 0.025$. This figure is qualitatively the same as Fig. 15(*c*), where, positions $q_2^{\pm}$, $q_3^{\pm}$ move apart from $x = 0$.

Figure 15(*e*) corresponds to $\hat{p}_2 = 0.06$. An inverted super critical bifurcation occurs when $\hat{p}_2^{cr} = 0.06$, where stable position q_0 becomes unstable on decreasing $\hat{p}_1$ and bifurcates into two stable states $q_1^{\pm}$. Saddle node bifurcations occurs at $p_1 = p_1^{cr}$ where positions $q_2^{\pm}, q_3^{\pm}$ are created.

Figure 15(*f*) corresponds to $\hat{p}_2 = 0.12$. This figure is qualitatively the same as Fig. 15 except that the inverted super critical bifurcation occurs at $\hat{p}_1$ values greater than $\hat{p}_1^{cr}$.

Note that in Figs. 15(*c*)–15(*f*), saddle node bifurcations of zero stiffness positions occur at lower values of $\hat{p}_1$ than for equilibrium positions.

6.3 Stiffness Diagrams. Mechanism stiffness at stable and unstable states is of great importance to compliant mechanism design [25]. Using Eq. (20), we calculate the effect of the programming inputs on the stiffness of equilibrium states and recall that the sign of the stiffness determines stability.

6.3.1 Equilibrium Position q_0. The equilibrium position q_0 exists for all $\hat{p}_1, \hat{p}_2$. When $\hat{p}_1 < \hat{p}_1^{cr}$, its stiffness $\hat{k}_{q_0}$ decreases with increasing $\hat{p}_2$. It is zero at $\hat{p}_2 = \hat{p}_2^{cr}$ and negative for $\hat{p}_2 > \hat{p}_2^{cr}$.

When $\hat{p}_1 > \hat{p}_1^{cr}$, the stiffness $\hat{k}_{q_0}$ decreases with increasing $\hat{p}_2$ reaching zero at $\hat{p}_2 = \hat{p}_2^{a}$. It is negative for $\hat{p}_2^{a} < \hat{p}_2 < \hat{p}_2^{b}$, zero at $\hat{p}_2 = \hat{p}_2^{b}$ and negative for $\hat{p}_2 > \hat{p}_2^{cr}$. Figures 16(*a*) and 16(*b*) illustrate k_{q_0} with respect to $\hat{p}_1$, $\hat{p}_2$.

6.3.2 Equilibrium Positions $q_1^{\pm}$. The equilibrium positions q_1^{+}, q_1^{-} are symmetric around $\hat{x} = 0$ and they exist when $\hat{p}_2 > \hat{p}_2^{cr}$. Their stiffness k_{q_1} is always positive, so they are stable. With $\hat{p}_1$ fixed, increasing $\hat{p}_2$ increases k_{q_1}. For $\hat{p}_2$ fixed, increasing $\hat{p}_1$ decreases k_{q_1}. Figures 16(*c*) and 16(*d*) illustrate k_{q_1} with respect to $\hat{p}_1$, $\hat{p}_2$.

6.3.3 Equilibrium Positions $q_2^{\pm}$. The equilibrium positions, q_1^{+}, q_1^{-} are unstable, symmetric around $\hat{x} = 0$ and they exist only when $\hat{p}_2 > \hat{p}_2^{b}$ and $\hat{p}_1 > \hat{p}_1^{cr}$. On increasing $\hat{p}_2$ for a given $\hat{p}_1$, their stiffness k_{q_2} decreases. Figures 16(*e*) and 16(*d*) illustrate k_{q_2} with respect to $\hat{p}_1$, $\hat{p}_2$.

6.3.4 Equilibrium Positions $q_3^{\pm}$. The equilibrium positions q_3^{+}, q_3^{-} are stable, symmetric around $\hat{x} = 0$ and they exit only when $\hat{p}_2 > \hat{p}_2^{a}$ and $\hat{p}_1 > \hat{p}_1^{cr}$. On increasing $\hat{p}_2$ for a given $\hat{p}_1$, their stiffness k_{q_3} increases. As p_1 increases and $\hat{p}_2$ is fixed, the magnitude of $\hat{k}_{q_3}$ increases. Figures 16(*g*) and 16(*f*) illustrate k_{q_3} with respect to $\hat{p}_1$, $\hat{p}_2$.

6.4 Special Cases. The T-mechanism exhibits near constant stiffness when the axial loads of its double parallelogram modules equal their zero stiffness loads. This leads to zero and constant force mechanisms [26].

We examine four cases with values illustrated in Fig. 17(*a*). We have made FEM simulations which validate the analytical model [21].

6.4.1 Zero Force Monostable Mechanism. When $\hat{p}_1 < \hat{p}_1^{cr}$ and $\hat{p}_2 = \hat{p}_2^{cr}$, the T-mechanism switches from monostability to bistability. The axial load of module 2 is equals its zero stiffness load [16]. The T-mechanism has a near zero reaction force in the range $-0.07 < \hat{x} < 0.07$ for $\hat{p}_1 = 0.0$, $\hat{p}_2 = 0.052$, as illustrated in Fig. 17(*b*).

6.4.2 Constant Force Monostable Mechanism. When the axial load on module 1 equals its zero stiffness load and $\hat{p}_2 < \hat{p}_2^a$, the mechanism is monostable and has regions of near constant force. Figure 17(*c*) illustrates the reaction force of the mechanism when $\hat{p}_1 = 0.012, \hat{p}_2 = 0$ with constant force range $-0.18 < \hat{x} < -0.13$ and $0.13 < \hat{x} < 0.18$, with $\hat{F} = -4.2$ and 4.2, respectively.

6.4.3 Zero Force Bistable Mechanism. When $\hat{p}_2 = \hat{p}_2^b$ and $\hat{p}_1 > \hat{p}_1^{cr}$, the mechanism switches from bistability to tristability. The axial load of module 2 equals its zero stiffness load, and the mechanism has near zero reaction force at $\hat{x} = 0$ leading to a zero force bistable mechanism. Figure 17(*d*) illustrates the reaction force of the mechanism at $\hat{p}_1 = 0.017$, $\hat{p}_2 = -0.045$, where the zero force range is $-0.03 < \hat{x} < 0.03$.

6.4.4 Constant Force Bistable Mechanism. When $\hat{p}_2 > \hat{p}_2^{cr}$ and $\hat{p}_1 < \hat{p}_1^{cr}$, the mechanism is bistable. When the axial load of module 1 equals its zero stiffness load, the mechanism has near constant force behavior. Figure 17(*e*) illustrates the reaction force of the mechanism at $\hat{p}_1 = 0.007$, $\hat{p}_2 = 0.092$, where the constant force ranges are $-0.31 < \hat{x} < -0.22$ and $0.22 < \hat{x} < 0.31$, with $\hat{F} = -0.13$ and 0.13, respectively.

6.4.5 Zero Force Tristable Mechanism. When $\hat{p}_1 > \hat{p}_1^{cr}$ and $\hat{p}_2 = \hat{p}_2^{cr}$, the mechanism switches from tristability to quadrastability. The axial load of module 2 equals its zero stiffness load. The mechanism has zero force behavior around $\hat{x} = 0$. Figure 17(*f*) illustrates the reaction force of the mechanism at $\hat{p}_1 = 0.017$, $\hat{p}_2 = 0.12$ with zero force range $-.03 < \hat{x} < 0.03$.

6.5 Degree of Stability Sensitivity. As demonstrated in Sec. 6.1, qualitative behavior is determined by the zeros of β_0, and this parameter is a polynomial in $\hat{p}_1$, $\hat{p}_2$, as given by Eq. (21) of Sec. 5.7, and is linear in $\hat{p}_1$ and cubic in $\hat{p}_2$. This gives smooth dependence on $\hat{p}_1$, $\hat{p}_2$ except at bifurcation points, i.e., DOS is locally constant.

Sensitivity to $\hat{p}_1$, $\hat{p}_2$ holds for the DOS at bifurcation points, since $\hat{p}_1$, $\hat{p}_2$ change continuously while the DOS is a discrete number. More generally, sensitivity of DOS at bifurcation is intrinsic to programmable multistable mechanisms since a discrete change occurs by continuous actuation [16].

Our model gives explicit formulas for bifurcation as function of programming input. Section 6.1 shows that bifurcation in $\hat{p}_1$ occurs at $\hat{p}_1^{cr}$ given by Eq. (37) and for $\hat{p}_2$ at zeros of β_0 at $\hat{p}_2^a, \hat{p}_2^b, \hat{p}_2^{cr}$.

7 Numerical Validation

COMSOL FEM was used to model the stability behavior of the 2DOP T-mechanism. Geometric nonlinearity was implemented by the solid mechanics module. Mesh convergence tests were performed to ensure the validity of solutions. Figure 18 illustrates the deformation of the mechanism for $\hat{p}_1 = 0.0$, $\hat{p}_2 = 0.12$.

Figure 19 gives the reaction force for monostable, bistable, tristable, and quadrastable configurations, calculated analytically and numerically. These data indicate that, for small $\hat{x}$, there is a good match between our analytical calculations and numerical simulations.

The discrepancy between the analytical and numerical models can reach 20%, as illustrated in Fig. 19(*f*). This is explained by having neglected the higher order nonlinear terms given in Ref. [27].

However, the analytical and numerical curves are qualitatively similar validating our qualitative analysis of stability behavior.

8 Applications

We give a brief overview of applications of programmable multistable mechanisms.

(1) Multistable mechanisms have been applied to computation. Logical operations were implemented using bistable mechanisms in Ref. [28]. Micromechanical computation devices have advantages over electronic circuits for low speed computations [29]. We conjecture that by using higher DOS, it is possible to realize a Turing complete mechanical computer. This is the subject of our current research.
(2) Threshold sensors have multiple stable states and they switch between them when sensing input exceeds threshold values, they have been used as acceleration, position, and shock threshold sensors [16,30]. Stability programming extends the threshold sensing concept to programmable sensors, where the number and the value of the threshold states are modifiable.
(3) This paper provide a new method for connecting bistable mechanisms to build programmable mechanical metamaterials [31], where the effective value of Young's modulus, the Poisson's ratio, and stable configurations can be controlled and stiffness estimated by our analytic model.
(4) Puncturing human tissue is required during surgery and necessitates great precision to avoid large forces causing irreversible damage. Stability programming provides control over puncturing force and stroke as we demonstrated in previous work [32].

9 Conclusion

We introduced the concept of stability programming and provided a novel analytic model of T-connected two degree of programming mechanisms yielding explicit expression for degree of stability, the position and stiffness of equilibrium states as well as estimates for constant force regimes. Our analysis was validated using FEM simulation.

We are currently working on the experimental validation as well as applications to mechanical computation using generalized T-combinations having higher degrees of programming.

References

[1] Harne, R., and Wang, K., 2013, "A Review of the Recent Research on Vibration Energy Harvesting Via Bistable Systems," Smart Mater. Struct., **22**(2), p. 023001.
[2] Younesian, D., and Alam, M.-R., 2017, "Multi-Stable Mechanisms for High-Efficiency and Broadband Ocean Wave Energy Harvesting," Appl. Energy, **197**, pp. 292–302.
[3] Oberhammer, J., Tang, M., Liu, A.-Q., and Stemme, G., 2006, "Mechanically Tri-Stable, True Single-Pole-Double-Throw (SPDT) Switches," J. Micromech. Microeng., **16**(11), p. 2251.
[4] Receveur, R. A., Marxer, C. R., Woering, R., Larik, V. C., and de Rooij, N.-F., 2005, "Laterally Moving Bistable MEMS DC Switch for Biomedical Applications," J. Microelectromech. Syst., **14**(5), pp. 1089–1098.
[5] Chen, G., Gou, Y., and Zhang, A., 2011, "Synthesis of Compliant Multistable Mechanisms Through Use of a Single Bistable Mechanism," ASME J. Mech. Des., **133**(8), p. 081007.
[6] Chen, G., Aten, Q. T., Zirbel, S., Jensen, B. D., and Howell, L. L., 2010, "A Tristable Mechanism Configuration Employing Orthogonal Compliant Mechanisms," ASME J. Mech. Rob., **2**(1), p. 014501.
[7] Oh, Y. S., and Kota, S., 2009, "Synthesis of Multistable Equilibrium Compliant Mechanisms Using Combinations of Bistable Mechanisms," ASME J. Mech. Des., **131**(2), p. 021002.
[8] Chen, G., Liu, Y., and Gou, Y., 2012, "A Compliant 5-Bar Tristable Mechanism Utilizing Metamorphic Transformation," *Advances in Reconfigurable Mechanisms and Robots I*, Springer, London, pp. 233–242.

[9] Chen, G., Zhang, S., and Li, G., 2013, "Multistable Behaviors of Compliant Sarrus Mechanisms," ASME J. Mech. Rob., **5**(2), p. 021005.
[10] Chen, G., and Du, Y., 2012, "Double-Young Tristable Mechanisms," ASME J. Mech. Rob., **5**(1), p. 011007.
[11] Halverson, P. A., Howell, L. L., and Magleby, S. P., 2010, "Tension-Based Multi-Stable Compliant Rolling-Contact Elements," Mech. Mach. Theory, **45**(2), pp. 147–156.
[12] Zhao, J., Huang, Y., Gao, R., Chen, G., Yang, Y., Liu, S., and Fan, K., 2014, "Novel Universal Multistable Mechanism Based on Magnetic—Mechanical—Inertial Coupling Effects," IEEE Trans. Ind. Electron., **61**(6), pp. 2714–2723.
[13] Howell, L. L., Magleby, S. P., and Olsen, B. M., 2013, *Handbook of Compliant Mechanisms*, Wiley, Hoboken, NJ.
[14] Cosandier, F., Henein, S., Richard, M., and Rubbert, L., 2017, *The Art of Exure Mechanism Design*, EPFL Press, Lausanne, Switzerland.
[15] Strogatz, S. H., 2014, *Nonlinear Dynamics and Chaos: With Applications to Physics, Biology, Chemistry, and Engineering*, Westview Press, Boulder, CO.
[16] Saif, M., 2000, "On a Tunable Bistable MEMS-Theory and Experiment," J. Microelectromech. Syst., **9**(2), pp. 157–170.
[17] Cazottes, P., Fernandes, A., Pouget, J., and Hafez, M., 2009, "Bistable Buckled Beam: Modeling of Actuating Force and Experimental Validations," ASME J. Mech. Des., **131**(10), p. 101001.
[18] Gerson, Y., Krylov, S., and Ilic, B., 2010, "Electrothermal Bistability Tuning in a Large Displacement Micro Actuator," J. Micromech. Microeng., **20**(11), p. 112001.
[19] Li, S., and Wang, K., 2015, "Fluidic Origami With Embedded Pressure Dependent Multi-Stability: A Plant Inspired Innovation," J. R. Soc. Interface, **12**(111), p. 20150639.
[20] Chen, G., Wilcox, D. L., and Howell, L. L., 2009, "Fully Compliant Double Tensural Tristable Micromechanisms (DTTM)," J. Micromech. Microeng., **19**(2), p. 025011.
[21] Zanaty, M., 2018, "Programmable Multistable Mechanisms," Ph.D. thesis, Ecole Polytechnique Federale de Lausanne, EPFL, Lausanne, Switzerland.
[22] Timoshenko, S. P., and Gere, J. M., 1961, *Theory of Elastic Stability*, McGraw-Hill-Kogakusha, Tokyo, Japan.
[23] Birkhoff, G., and Mac Lane, S., 1966, *A Survey of Modern Algebra*, CRC Press, Boca Raton, FL.
[24] Bensimhoun, M., 2016, "Historical Account and Ultra-Simple Proofs of Descartes's Rule of Signs, De Gua, Fourier, and Budan's Rule," e-print arXiv:1309.6664.
[25] Howell, L. L., 2001, *Compliant Mechanisms*, Wiley, Hoboken, NJ.
[26] Herder, J., 2001, "Free Energy System: Theory, Conception and Design of Statically Balanced Spring Mechanisms," Ph.D. thesis, Delft University of Technology, Delft, The Netherlands.
[27] Hao, G., 2015, "Extended Nonlinear Analytical Models of Compliant Parallelogram Mechanisms: Third-Order Models," Trans. Can. Soc. Mech. Eng., **39**(1), pp. 71–83.
[28] Merkle, R. C., 1993, "Two Types of Mechanical Reversible Logic," Nanotechnology, **4**(2), p. 114.
[29] Hafiz, M., Kosuru, L., and Younis, M. I., 2016, "Microelectromechanical Reprogrammable Logic Device," Nat. Commun., **7**, p. 11137.
[30] Gomm, T., Howell, L. L., and Selfridge, R. H., 2002, "In-Plane Linear Displacement Bistable Microrelay," J. Micromech. Microeng., **12**(3), p. 257.
[31] Rafsanjani, A., Akbarzadeh, A., and Pasini, D., 2015, "Snapping Mechanical Metamaterials Under Tension," Adv. Mater., **27**(39), pp. 5931–5935.
[32] Zanaty, M., Rogg, A., Fussinger, T., Lovera, A., Baur, C., Bellouard, Y., and Henein, S., 2017, "Safe Puncture Tool for Retinal Vein Cannulation," Design of Medical Devices (DMD), Eindhoven, The Netherlands, Nov. 14–15.